A bench-top K x-ray fluorescence system for quantitative measurement of gold nanoparticles for biological sample diagnostics

Ricketts, K.[a], Guazzoni, C. [b], Castoldi, A. [b], Royle, G.[c]

[a]Division of Surgery and Interventional Sciences, University College London, Royal Free Campus, Rowland Hill Street, London, NW3 2PF, UK

[b]Dipartimento di Elettronica, Informazione e Bioingegneria Politecnico di Milano and INFN, Sezione di Milano P.za Leonardo da Vinci, 32 - 20133 Milano, Italy

[c]Department of Medical Physics and Bioengineering, University College London, Malet Place Engineering Building, Gower Street, London, WC1E 6BT, UK

Corresponding author:

Dr Kate Ricketts

Division of Surgery and Interventional Sciences, University College London,

Royal Free Campus, Rowland Hill Street, London, NW3 2PF, UK

Email: k.ricketts@ucl.ac.uk

Tel: +44 (0)207 794 0500 ext: 37665

Fax: +44 (0)207 472 6444

Key words: Nanoparticles, x-ray fluorescence, biomarkers

Abstract

Gold nanoparticles can be targeted to biomarkers to give functional information on a range of tumour characteristics. X-ray fluorescence (XRF) techniques offer potential quantitative measurement of the distribution of such heavy metal nanoparticles. Biologists are developing 3D tissue engineered cellular models on the centimetre scale to optimise targeting techniques of nanoparticles to a range of tumour characteristics. Here we present a high energy bench-top K-x-ray fluorescence system designed for sensitivity to bulk measurement of gold nanoparticle concentration for intended use in such thick biological samples. Previous work has demonstrated use of a L-XRF system in measuring gold concentrations but being a low energy technique it is restricted to thin samples or superficial tumours. The presented system comprised a high purity germanium detector and filtered tungsten x-ray source, capable of quantitative measurement of gold nanoparticle concentration of thicker samples. The developed system achieved a measured detection limit of between 0.2 – 0.6 mgAu/ml, meeting specifications of biologists and being approximately one order of magnitude better than the detection limit of alternative K-XRF nanoparticle detection techniques. The scatter-corrected K-XRF signal of gold was linear with GNP concentrations down to the detection limit, thus demonstrating potential in GNP concentration quantification. The K-XRF system demonstrated between 5 and 9 times less sensitivity than a previous L-XRF bench-top system, due to a fundamental limitation of lower photoelectric interaction probabilities at higher K-edge energies. Importantly, the K-XRF technique is however less affected by overlying thickness, and so offers future potential in interrogating thick biological samples.

1 Introduction

Gold nanoparticles (GNPs) have considerable potential in biomedical applications. Their small size and surface chemistry enables conjugation to antibodies to target biomarkers [1] and encapsulation to minimise toxicity [2]. Bio-conjugation with targeting antibodies elicits uptake ten times that of healthy cells [3]. GNPs can be taken up into cells through mechanisms including endocytosis [4], [5] offering drug delivery potential [6]. They can be tailored for use as contrast agents in functional imaging (Jiao et al. 2011), and for targeted tumour dose enhancement in radiotherapy [8], [9].

GNPs are an ideal contrast medium for use in x-ray imaging techniques, gold being of high atomic number and therefore more absorptive than surrounding tissue, providing better contrast with potentially lower dose [10], [11]. An important performance criteria of GNP tumour detection systems is sensitivity to low concentrations of GNPs that are expected in the 3D biological samples. The expected tumour GNP concentration is dependent upon many factors, including those that influence in vivo NP transport and cell uptake (GNP size and coating) [3], and GNP incubation dose. To date work has almost exclusively focused on the use of NPs and attachment of required molecules, with resulting uptake and effect studies limited to oversimplified 2D cellular models or animal models which are not conducive to detailed mechanistic investigations. Biologists and tissue engineers are developing 3D cellular / stromal models of centimetre scale with potential to quantify and optimise GNP targeting efficiency under controlled cellular conditions [12]. This study proposes a high energy K-XRF system with capability of bulk measurement of GNP concentration within such thick biological samples to determine GNP cellular uptake. Biologists require a quantitative non-imaging modality to probe GNP concentration of samples fixed at different timepoints; the fixing process kills the sample and so radiation dose is not an issue and so was not considered in this system.

In order to achieve biological sample GNP levels that are clinically appropriate, the literature was probed to determine typical in vivo GNP concentrations in imaging and radiation enhancement

studies. Such studies have demonstrated a range of tumour GNP concentrations (0.07 – 6.4 mgAu/ml) [11], [13], [14], [15]. The wide range of measured tumour GNP concentration is primarily related to the range of GNP administration doses (0.036 – 1.35 mgAu/g (mouse)), as well as commonly accepted factors relating to nanoparticle coating and size.

A number of systems have reported potential in GNP concentration measurement, each offering different detection limits (the lowest GNP concentration that can be quantitatively measured). The Herceptin-targeted GNP study used microCT for quantification of GNPs within various regions of a murine tumour; they report that the sensitivity of a 140 kVp CT broad spectrum beam of mean energy 70 keV has theoretical potential to give a minimum detectable level of 0.5 mgAu/ml [11]. In addition, x-ray fluorescence solutions have been offered, whereby the magnitude of the XRF signal is proportional to the concentration of that element, and the energy of the fluorescence indicates elemental composition (enabling multi-parametric imaging). XRF is typically performed using narrow spectral widths, such as those from a synchrotron, in order to benefit from the photoelectric absorption edge of the material. However, synchrotron sources are not practical for routine clinical measurement. In previous work we developed an L-XRF system capable of quantifying GNP concentrations down to 1ppm (0.005 mgAu/ml) through use of a bench-top molybdenum x-ray tube, polycapillary optics and a silicon drift detector (SDD) [16]. From our knowledge this remains the most sensitive XRF system to GNP detection within the literature, with a competitive L-XRF system achieving a detection limit of 0.02 mgAu/ml [17]. Our sensitive system was used for 2D quantitative imaging of GNP distribution using GNP-loaded phantoms [18] and 3D quantitative imaging of cellular nanoparticle uptake tumour models [5].

However L-XRF systems are limited to GNP detection at shallow sites. In order to perform GNP fluorescence analysis at depth, higher energy incident and XRF x-rays are required to penetrate through overlying tissue. The K-absorption edge of gold lies at 80.7 keV, and so a higher energy source is required to induce K-XRF. In addition to this, a detector more suited to detecting higher energy x-rays is required. Therefore translation to a K-XRF system involved: (i) replacing the SDD from our L-XRF system with a high energy x-ray detector, and (ii) replacing the molybdenum x-ray source with a higher energy source. Gold XRF characteristics are displayed in Table 1.

Table 1 Theoretical energies and yields of the gold K-XRF and L-XRF emissions [19].

	$K_{\alpha 1}$	$K_{\alpha 2}$	$K_{\beta 1}$	$L_{\alpha 1}$	$L_{\alpha 2}$	$L_{\beta 1}$	$L_{\beta 2}$	$L_{\gamma 1}$
Energy (keV)	68.80	66.99	77.98	9.71	9.63	11.44	11.58	13.38
Emission relative to $K_{\alpha 1}$ (%)	100	59	23	37	4	25	8	4
Absorption edge energy (threshold energy for fluorescence) (keV)	80.7	80.7	80.7	11.9	11.9	13.7	11.9	13.7

A number of K-XRF GNP detection systems are presented in the literature, but none have demonstrated detection limits capable of detecting GNP concentrations towards the lower end of the range expected in tumours (~0.1 mgAu/ml). A number of x-ray fluorescence computed tomography (XFCT) imaging studies of GNP-loaded phantoms have been demonstrated using a diagnostic (110 kVp) pencil-beam source to induce K-XRF in gold and a CdTe detector [20], [21], [22]. Relatively

high GNP concentrations were tested by the systems, and reported detection limits ranged from 10 mgAu/ml [21] down to 2 mgAu/ml [22]. A Monte Carlo study reported that the best theoretically possible K-XFCT detection limit using a polychromatic source was 1 mgAu/ml [23].

Here we present a K-XRF system that offers greater sensitivity through optimised implementation of a high purity germanium detector and tungsten polychromatic bench top source that could be used for quantitative measurement of GNP concentration at depth.

2 Materials and Methods

2.1 GNP samples

The samples consisted of GNPs (Aurovist™, Nanoprobes Inc., USA) suspended in a 1 ml de-ionized water buffer. The GNPs used had a 1.9 nm gold core and water-soluble organic shell. Each sample solution was held in a plastic 1.5 ml Eppendorf tube (Eppendorf, Germany) of internal diameter 8 mm and height 45 mm. Sample concentrations ranged from 0.2 to 8 mgAu ml^{-1} (made to an accuracy of ±1%) for K-XRF measurement, to test the minimum detectable concentration. A micro-pipetter that can measure volumes to the nearest 1 µl was used, and a four-stage dilution technique ensured that the GNP residue remaining behind in the GNP storage container was negligible. A 1 ml de-ionized water sample was measured for background data.

2.2 Bench-top K-XRF system

The K-XRF system consists of a collimated high purity germanium (HPGe) detector. An x-ray beam irradiated the sample and the HPGe detector was placed at 90° to the incident beam beside the sample (Figure 1).

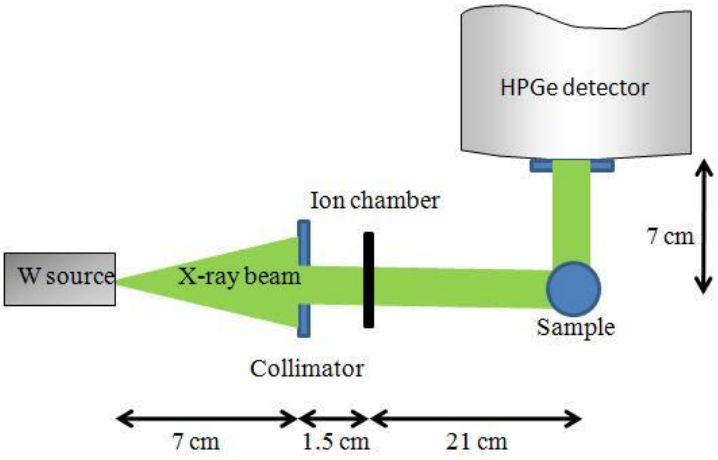

Figure 1 Experimental set-up of bench-top K-XRF measurement system, viewed from above. Beam collimator comprised of lead-backed aluminium (2 mm Pb, 2 mm Al) of dimensions 1.5 mm high and 1.5 mm wide. Detector collimator comprised of a custom made lead shield of circular aperture 10 mm diameter.

2.2.1 X-ray source

The $K\alpha_1$ fluorescence at 68.8 keV was the dominant emission and so the system was designed to increase sensitivity to this energy. The selection of excitation source was governed by: (i) requirement of a photon energy that is greater than, but as close as possible to, the gold K-edge at 80.7 keV in order to overcome the binding energy of the K-electrons and thus maximise the gold XRF yield, (ii) the source should have as narrow a spectral width as possible in order to minimise the background due to scatter in the gold fluorescence peaks region.

An industrial water-cooled x-ray tube (AGO installations, Philips) was used with rotating tungsten anode of nominal focal spot size 3 mm x 3 mm, and inherent filtration of 1 mmBe. It ran in continuous mode at 120 kV_p and 1 mA. A specially designed lead collimating circular window of 5 mm diameter was mounted onto the front of the x-ray tube to act as an initial coarse collimator to reduce x-ray scatter in the room.

Simulations were performed to optimise filtration parameters for compromise between narrow spectral width and x-ray intensity, attenuating unwanted wavelengths below the threshold for gold K-flourescence (80.7 keV). The K-absorption edge of lead (88.2 keV) offered beam shaping potential. SpekCalc [24] was used to simulate an x-ray spectrum from a tungsten source set at 120 kV_p, 30° anode angle, 1 mmBe inherent filtration (according to the specification of the x-ray unit used in these measurements). An inverse square law correction was used to calculate the spectrum at the position of the sample (70 mm from the source). The number of incident x-rays involved in a photoelectric interaction (I_{PE}) and which may therefore contribute to an XRF event was theoretically determined:

$$I_{PE} = \sum_{E_{edge}}^{E\max} I_0(E)(1-e^{-\sigma(E)x}) \qquad \text{Equation 1}$$

where $I_0(E)$ is the number of incident x-rays of energy E and $\sigma(E)$ is the photoelectric cross section at E. E_{edge} corresponds to the energy threshold for fluorescence (80.7 keV for K-XRF). A power fit was used to interpolate values of gold attenuation coefficients [25].

The 'useful' proportion of the total incident beam R_{XRF} was calculated as the ratio of the number of incident x-rays that contribute to a photoelectric interaction against the total number of incident x-rays (Equation 2):

$$R_{XRF} = \frac{I_{PE}}{\sum_{E=0}^{E_{\max}} I_0} \qquad \text{Equation 2}$$

To verify simulation, a series of measurements of spectral width and intensity were made over a range of lead filter thicknesses.

2.2.2 X-ray detector

The silicon drift detector (SDD) was an ideal detector for use in L-XRF measurement; its high energy resolution (138 eV FWHM at a shaping time of 1μs at 5.9 keV and a maximum count rate of the order of 10^5 s^{-1}) and low noise gave high performance in measuring very low GNP concentrations down to 1 ppm [16]. However, the detection module was made of a 450 μm thick silicon substrate rendering it inefficient at absorbing and detecting high energy x-rays. For K-XRF measurement the

SDD was replaced with a high purity germanium (HPGe) detector (EG&G Ortec) of active depth 7 mm which was more efficient at K-XRF energies (99.7% efficiency of detection of the gold $K\alpha_1$ 68.8 keV). The HPGe detector consisted of a single planar germanium crystal of diameter 36 mm enclosed in a vacuum with a 0.254 mm thick beryllium window, and operated under liquid nitrogen temperatures. Spectrum Master 92X Multi Channel Analyser and Maestro 32 software (EG&G Ortec) was used to analyse the energy spectrum. The energy resolution of the HPGe detector was measured to be less than 0.7 keV at 59.5 keV using an Americium-241 source. The detector was encased in a purpose built lead x-ray shield with a circular aperture of diameter 10 mm on the front face of the detector, concentric with the Ge crystal. This acted to shield from unwanted multiple scatter x-rays and to minimise the detector dead time. The dead time of the HPGe detector was below 10% at all times; greater dead times could result in pulse pile-up of the x-ray counts and warp the energy spectrum.

2.2.3 Collimation and measurement geometry

An ideal XRF system uses a collimated parallel x-ray beam to ensure incidence only on the sample to: (i) avoid inducing fluorescence in other materials present in the system, (ii) minimise the background scatter contribution to the detected spectrum, and (iii) benefit from Compton reduction in a 90° detection geometry. However, bench-top x-ray tubes produce a diverging beam. For the L-XRF bench-top system, this problem was solved through use of polycapillary x-ray technology to convert the diverging beam in to a parallel beam, and the beam collimated to 3.4 mm wide by 1.5 mm high to cover the uniform area of the beam exiting the polycapillary optic. However for the higher energy K-XRF source, polycapillary optic techniques could not be implemented as the high energy x-rays would penetrate through the glass capillary fibres rather than being channelled between them. Therefore, a more divergent incident beam (beam divergence 1.5°) and higher scatter background was present for the case of K-XRF. A beam collimator comprised of lead-backed aluminium (2 mm Pb, 2 mm Al) of dimensions 1.5 mm high and 1.5 mm wide was used to give a beam area of 91.5 mm x 91.5 mm at the sample position, fully covering the sample laterally to meet design aims of bulk measurement of GNP concentration of the sample.

For this reason the K-lines of potential system materials were reviewed to identify potential interference issues with the K-lines of gold: the threshold energy for K-fluorescence was 80.7, 69.5 and 88.0 keV for gold, tungsten and lead respectively. Fluorescence lines of lead (74.96, 72.79, 84.92 keV) and tungsten (59.31, 57.97, 67.23 keV) were very similar to gold K-lines (68.8, 66.99, 77.98 keV for $K\alpha_1$, $K\alpha_2$ and $K\beta_1$ respectively. The smallest difference between the significant K-lines of tungsten and gold was 0.24 keV (gold $K\alpha_2$ – tungsten $K\beta_1$); this difference could not be resolved by the HPGe detector (measured energy resolution of 0.7 keV at 59.5 keV). Primary beam incidence on the detector was eliminated through use of (i) a 90° detection geometry, and (ii) detector shielding and so use of a tungsten target was acceptable. However, Compton scattered tungsten $K\alpha$-peaks were detected, but the scatter process reduced the energy of the tungsten lines away from the gold signal. Lead XRF lines were at an energy that could be resolved from the gold signal using the HPGe detector, and so posed no problems.

Sample-detector distance was minimised (70 mm distance) in order to maximise the detection of the isotropically emitted XRF signal. Closer distances were not possible due to practical limitations in the experimental set-up. A complementary metal-oxide-semiconductor (CMOS) sensor was located behind the sample to monitor the beam-sample alignment, and an ionisation chamber was used to correct for changes in incident beam intensity.

2.2.4 Measurement procedure

The time duration of spectra collection was set to keep the counting statistics error of the fluorescence peak below 1% for each sample concentration measured. A measurement time of 1200s provided sufficient counting statistics. Ion chamber readings were recorded for each acquisition to correct for tube intensity variation between measurements.

2.2.5 Measurement at depth

The effect of overlying material on nanoparticle detection was investigated for the K-XRF system. A series of XRF measurements of an 8 mgAu/ml GNP sample with a range of thicknesses of Perspex (0 - 15 mm) fully surrounding the sample. Perspex has similar attenuating properties to tissue at these energies.

2.3 Data analysis

2.3.1 Isolation of gold K-XRF signal

An example of a measured K-XRF spectrum is displayed in Figure 4. A region covering the $K\alpha_1$ and $K\alpha_2$ peaks was selected for analysis (those lines being the strongest present in the range of concentrations measured). A 2-order polynomial least squares fit gave the best fit to the background non-peak regions, and was interpolated to give an estimate of the background signal under each gold XRF peak (an example background fit is displayed in Figure 2).

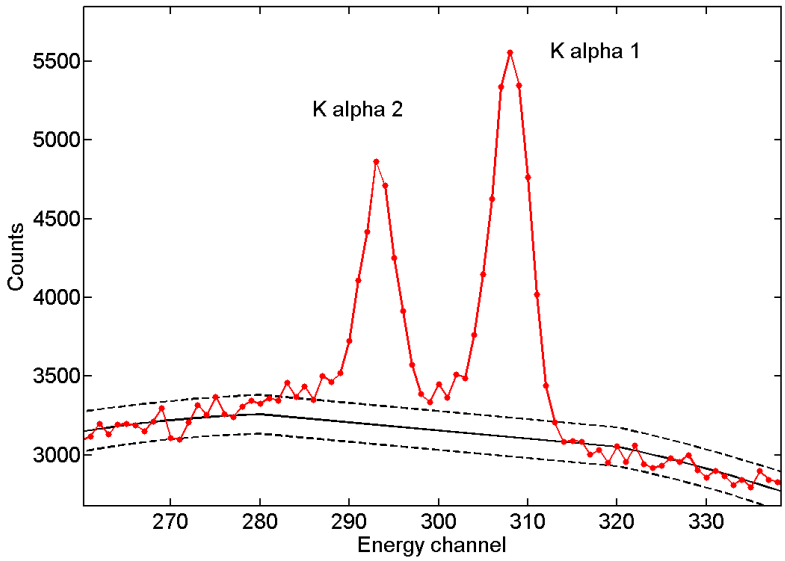

Figure 2 Data surrounding the gold Kα peaks. A background fit (solid line) gives the background beneath each gold fluorescence peak. The 95% confidence levels to the background fit are displayed as the dashed lines.

The background fit (B_i) was subtracted from the measured peak counts (P_i) to isolate the gold XRF signal (F_i). A Gaussian was fitted to each prominent gold K-line ($K\alpha_1$ and $K\alpha_2$). The XRF signals were normalised to incident beam intensity and acquisition time. The HPGe detector energy to channel number calibration was found to drift over time. The XRF analysis was modified to

account for the drift in the position of XRF peaks by giving a degree of freedom to the peak position of the Gaussian fit. This was not required for the L-XRF measurements.

2.3.2 Absorption and geometry correction techniques

Previous studies have shown that radiation Compton scattered by the sample can be used as an internal standard to correct for the effects of self-absorption and geometrical variations on the measured XRF signal [26], [27]. Scatter normalisation will also correct for any small changes in source-sample or sample-detector distance errors in sample positioning. The Compton peak of the tungsten $K\alpha_1$ line was used to perform this correction for the K-XRF bench-top system. The resulting scatter corrected fluorescence signal I_{FS} is:

$$I_{FS} = \frac{I_{net}}{I_C} \qquad \text{Equation 3}$$

where I_{net} is the sum of the background-subtracted Gaussian-fitted XRF peak data, and I_C is the intensity of the Compton-scattered x-rays. The scatter correction technique was previously tested over five repeat sample measurements and found to give a standard deviation of the measured gold XRF signal over all measurements of 1.6% compared to 9.1% without the scatter correction [16].

2.3.3 Measures of system performance

The same figures of merit were used to evaluate the performance of the K-XRF system in GNP concentration measurement as for previous work with L-XRF systems [16]. In summary:

(i) The detection limit (DL) is a measure of the capability of the system to distinguish a true net peak intensity (taken as the peak height P of the Gaussian fit to the gold XRF peaks) from the random fluctuations of the background signal. The background noise (σ_b) was taken to be the standard deviation of the data points about the background least-squares fit. The magnitude of P must be at least 1.96 σ_b to be able to distinguish the net fluorescence signal from statistical fluctuations with a 95% confidence level. It follows that the DL can be determined by finding the concentration at which $P/\sigma_b = 1.96$.

(ii) The sensitivity was calculated by finding the gradient of a linear fit of XRF signal against GNP concentration with no correction for beam intensity or self-attenuation to enable direct comparison of the two systems.

(iii) Accuracy of GNP concentration measurement was assessed: A weighted linear least-squares fit was applied to the XRF signal measured at each concentration above the detection limit. A weighting w_i was applied to the ith measurement of magnitude

$$w_i = \frac{1}{E_i^{\,2}} \qquad \text{Equation 4}$$

where E_i is the error of the ith XRF signal measurement and was calculated by summing in quadrature the statistical error in the gold and scatter signals. The error in the gradient of the linear fit determined the accuracy with which the GNP concentration can be measured.

3 Results

3.1 Filtration optimisation

Simulations demonstrated that introduction of 0.5 mm Pb and 1 mm Pb filtration to the K-XRF system yielded a 2.6 and 3.8 times greater useful proportion of the incident beam respectively than when used without filtration (Table 2). However, the rate of K-XRF production reduced by a factor of 6.2 and 21.6 when using these filter thicknesses due to the decrease in intensity (Table 2). Figure 3 demonstrates the simulated effect of using different thicknesses of lead filter upon spectral shape; the characteristic tungsten lines were reduced as lead thickness increased. This was beneficial as the tungsten lines would have contributed to the detector dead time without contributing to the gold XRF production. It can be seen that the spectral width of the spectrum became narrower with increasing lead thickness, as supported by measured results (Table 2).

After consideration of all factors it was decided that a 0.5 mm lead filter and tube setting of 120 kV_p gave a compromise between lowering the background beneath the gold signal and keeping the rate of XRF production sufficiently high.

Table 2 Simulated useful portion of the beam R_{XRF} (ratio of the number of incident x-rays that contribute to a photoelectric interaction against the total number of incident x-rays), measured spectral width (expressed as full width at half maximum (FWHM)) and measured minimum energy of filtered x-ray spectrum, across a range of lead filter thicknesses.

Filter thickness (mmPb)	R_{XRF} (for x-rays passing through 0.1 mm gold) (simulation)	Spectral width (FWHM, keV) (measurement)	Low energy cut-off (keV) (measurement)
0	0.8%	-	-
0.5	2.0%	24.5	41.1
1	3.0%	16.2	47.9
1.5	3.9%	12.6	54.4
2	4.6%	10.0	58.6

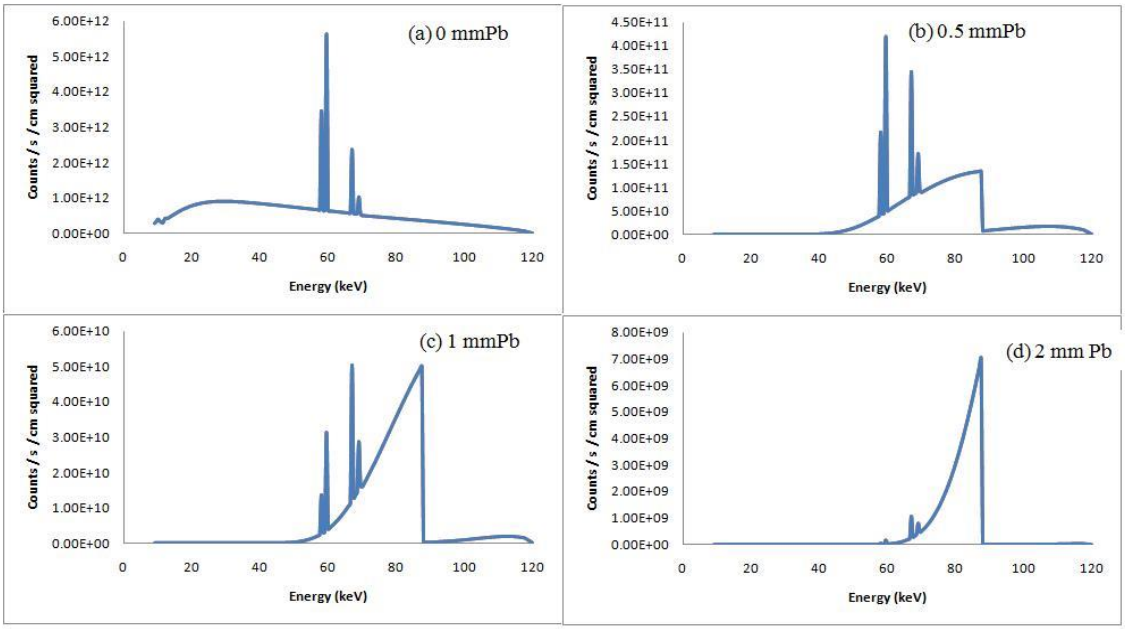

Figure 3 Simulated spectral shape of x-ray beam at tube voltage 120 kV_p with a range of lead filter thicknesses.

3.2 Measured spectra

An example measured spectrum from the K-XRF bench-top system is displayed in Figure 4. The gold Kα and Kβ lines were clearly distinguishable from the down scattered tungsten Kα lines.

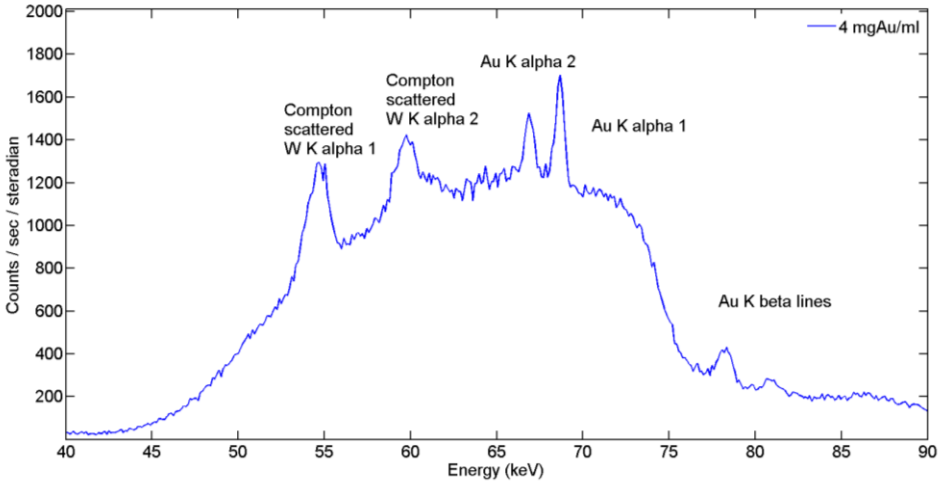

Figure 4 Measured K-XRF spectrum of a 4 mgAu/ml GNP sample (1200s).

3.3 Detection limit and sensitivity

The measured GNP detection limit and sensitivity of the K-XRF system is displayed in Table 3. It can be seen that this system offers greater sensitivity than other systems present in the literature, with a detection limit between 0.2 – 0.6 mgAu/ml, thereby above the minimum theoretical detection limit of XFCT of 1 mgAu/ml [23]. The $K\alpha_1$ peak analysis produced the lowest DL, having a greater yield

than the $K\alpha_2$ line. Two-peak analysis yielded a greater sensitivity than using either sole peak; this is due to the increase in signal intensity upon summing both peaks together.

Table 3 Detection limits and sensitivity of K-XRF bench-top system at a 95% confidence level

	Detection limit (mgAu/ml)	**Sensitivity (XRF peak counts per mgAu/ml per second per solid angle)**
$K\alpha_1$	0.2 < DL < 0.6	~400 ± 20%
$K\alpha_2$	0.6 < DL < 2.0	~700 ± 18%
$K\alpha_1 + K\alpha_2$	0.2 < DL < 0.6	~1100 ± 15%

3.4 Accuracy of GNP concentration measurement

Figure 5 displays the weighted least-squares linear fit and associated 95% confidence levels of the scatter-corrected K-XRF signal against GNP concentration. The K-XRF system could measure GNP concentration to within ± 0.02 mgAu/ml at concentrations between the detection limit and 2 mgAu/ml.

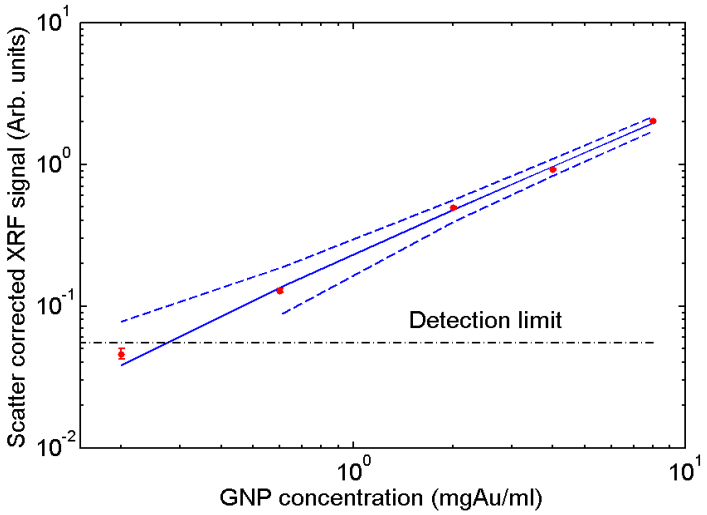

Figure 5 Weighted least squares linear fit (solid line) of XRF signal over a range of measured GNP concentrations using the K-XRF bench-top source. 95% confidence levels of the linear fit are displayed as dashed lines, and the detection limit plotted.

3.5 Measurement at depth

The effect of surrounding Perspex thickness to the K-XRF bench-top system spectra is displayed in Figure 6. All gold signals were found to be above the DL of the system. The measured reduction in both the gold Kα1 and Kα2 signals due to surrounding Perspex thickness is tabulated in Table 4. An

80% decrease in detectability of the 8mgAu/ml sample was found when surrounded by 15 mm Perspex.

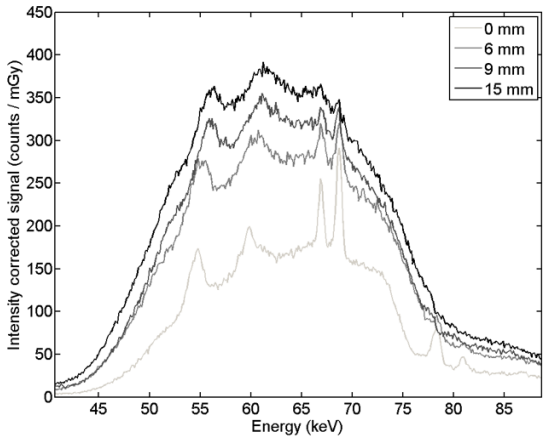

Figure 6 Measured K-XRF spectra of an 8 mgAu/ml sample acquired with a range of Perspex thicknesses surrounding the sample. Each spectrum was normalized to the x-ray dose measured by an ion chamber in the beam.

Figure 6 displays an increased background scatter component with increasing Perspex thickness for the K-XRF system. This background originated from scatter interactions with the Perspex as the x-rays exited the sample; the thicker the Perspex, the greater the number of scatter interactions. This increased the number of x-rays reaching the detector. A larger background component made it more difficult to see the XRF signal from lower concentrations. An increase in unwanted background counts also acted to increase the detector dead time, which had a negative impact on the measurement by increasing required acquisition time and also led to distortion of the measured spectrum.

Table 4 Effect of Perspex thickness surrounding an 8 mgAu/ml sample on measured background-subtracted K-XRF signals

Perspex thickness	**Gold Kα1 reduction (%)**	**Gold Kα2 reduction (%)**
6 mm	50%	49%
9 mm	65%	64%
15 mm	80%	74%

4 Discussion

A K-XRF system was successfully designed and implemented for sensitivity to GNP concentration measurement at levels and sample thicknesses appropriate to centimetre scale 3D biological samples. Each component of the system was optimised in order to achieve a low detection limit of between 0.2 – 0.6 mgAu/ml. This system was designed for bulk quantitative GNP measurement and not for imaging, and thus has a better detection limit compared with the theoretical limits of XFCT (1 mgAu/ml) [28] and microCT (0.5 mgAu/ml) [11]. The scatter-corrected K-XRF signal of gold was

linear with the tested GNP concentrations down to the detection limit, thus demonstrating potential in GNP concentration quantification.

The high energy resolution of the high purity germanium module is a major contributor to the good performance of the K-XRF system, not only in terms of being able to resolve the x-rays of each fluorescence peak but also in giving a low DL. Competitive techniques within the literature implemented a CdTe detector which has energy resolution typically a factor of 2 or more poorer than HPGe. To achieve a low DL, the XRF peak must be easily visible above the background upon which it sits. The energy deposited by an x-ray is represented by the area of the whole peak. If a sample containing a certain amount of gold is measured using two detectors of differing energy resolution R (where R = FWHM of the fluorescence peak), for the peak area to remain constant, a wider peak (poorer R) must be smaller, and a narrower peak (better R) must be taller. The DL also improves as detection time is increased, until the instrumental error (in this case the detector electronic noise) dominates above statistical noise. The electronic noise charge of the SDD is very low at 8.3 electrons for a 1 μs shaping time, enabling very low detection limits.

An 84% decrease in detectability of the 8 mgAu/ml sample was found when surrounding the GNP sample with 15 mm Perspex. Similar measurements were previously presented for a synchrotron based L-XRF system, whereby layers of Perspex were added between the sample and detector: 16 mm Perspex gave a 99.2% and 88.8% reduction in the detectability of the $L\alpha$ and $L\beta$ signals respectively [18]. A Perspex geometry similar to that used in the L-XRF measurements would bring about a much lower decrease, as the incident beam would not have been attenuated. It can be concluded that the K-XRF technique is less affected by overlying thickness than the L-XRF technique, as expected.

Further comparison to the L-XRF system showed that the count rate of the gold peaks using the L-XRF bench-top system was approximately six times that of the K-XRF bench-top system for a 4 mgAu/ml sample. The background beneath the gold signal of the K-XRF system was much greater than for either of the L-XRF systems [16]. This combined with the lower peak count rate made the K-XRF system far less sensitive to low GNP concentrations.

The three XRF systems have been compared in terms of sensitivity, accuracy of measurement and minimum detectable limit. Sensitivity was corrected for the differing beam / detector geometries between each system through normalising to solid angle. The key results of all three systems are summarised in Table 5.

Table 5 Summary of key results in order to compare the performance of each XRF system (L-XRF measurements from previous work [16]*).*

	L-XRF synchrotron source	**L-XRF bench-top source**	**K-XRF bench-top source**
Detection limit (mgAu/ml)	< 0.008	0.005	0.2 < DL < 0.6
Sensitivity (XRF peak counts per mgAu/ml per second per solid angle)	~182,700 ± 6%	~7300 ± 7%	~1100 ± 15%
Uncertainty (mgAu/ml)	± 0.005	± 0.005	± 0.02
(for concentration range)	(DL – 0.1 mgAu/ml)	(DL – 0.1 mgAu/ml)	(DL – 2 mgAu/ml)

The sensitivity defined as the measurable XRF signal per unit GNP concentration is affected by both the intensity and spectral shape of the x-ray source. The L-XRF bench-top system was found to be between 5 - 9 times more sensitive than the K-XRF bench-top system (depending on which peaks were used for analysis). The primary contributing factor for this difference in performance is the difference in photoelectric interaction cross section: the photoelectric cross section just above the L-edge of gold (σ (11.98 keV) = 179.11 cm^2/g) is over 21 times greater than that just above the K-edge (σ (81.13 keV) = 8.2842 cm^2/g) (values taken from [25]). However, the fluorescence yields are also different for K and L fluorescence; the $K\alpha_1$ and $K\alpha_2$ emission rate is 2.15 times greater than for $L\alpha$ and $L\beta$ emission. These two factors together make L-XRF a factor of 9 more likely to occur than K-XRF. This corroborates with our measured result of the L-XRF system having 5 – 9 times more sensitivity than the K-XRF system. Also, the ratio of photoelectric cross section to total scatter cross section (corresponding to signal to noise ratio) is greater for L-XRF than K-XRF (ratios of 43.4 and 22.0 at the L-edge and K-edge energies respectively). This means that the scatter contribution to the background beneath the gold signal for the K-XRF system is double that for the L-XRF system, making it less sensitive to low concentration measurement.

A confounding factor is that the intensity of the K-XRF source was greater than the L-XRF source; however this cannot be directly attributed to the difference in sensitivity because the spectral shape must also be considered. Use of an optimum source energy just above the absorption edge of gold increases the photoelectric cross section and so will increase the rate of emission of XRF x-rays. Increasing the source intensity increases both the background and the peak counts equally, whereas optimising the spectral shape can result in increasing the number of peak counts whilst reducing the background. Beam filtration (0.5 mm lead) was used in the K-XRF system to optimise the spectral shape, but this involved a compromise with beam intensity and resulted in longer acquisition times to achieve the same counting statistics. Further improvements would be possible through use of a higher intensity source with a greater thickness lead filter. In addition future implementation of a crystal monochromator to convert the polyenergetic beam to a quasi-monochromatic beam would offer potential in improving performance.

5 Conclusions and future work

A K-XRF system was successfully designed and implemented for sensitivity to GNP concentration. A measured detection limit of between 0.2 – 0.6 mgAu/ml met biological specifications of GNP cellular uptake measurement, being almost one order of magnitude better than the limit of alternative K-XRF techniques. This was attributed to the high performing energy resolution of the detector used. The scatter-corrected K-XRF signal of gold was linear with the tested GNP concentrations down to the detection limit, thus demonstrating potential in GNP concentration quantification. The K-XRF system demonstrated between 5 and 9 times less sensitivity than a previous L-XRF bench-top system. The sensitivity of K-XRF is fundamentally limited by lower photoelectric interaction probabilities at higher K-edge energies, and a higher spectral background contribution. The K-XRF technique is however less affected by overlying thickness, and so meets the design criteria in interrogating centimetre scale tissue engineered biological samples and also offers future potential in interrogating thick ex vivo biopsy samples.

6 Acknowledgments

The authors are indebted to Katherine Holt of the UCL Department of Chemistry for her assistance in nanoparticle sample preparation. We would like to thank Christiana Christodoulou and Sangeeta Maini for their assistance in the x-ray laboratory, and Joe Evans from the Medical Physics Department at UCL for his workshop support.

7 References

[1] R. Popovtzer, A. Agrawal, N. Kotov, A. Popovtzer, J. Balter, T. Carey, et al., Targeted Gold Nanoparticles Enable Molecular CT Imaging of Cancer, Nanoletters. 8 (2008) 4593–4596. doi:10.1021/nl8029114.

[2] R. Kemp, M., Linhardt, Heparin-based nanoparticles, Wiley Interdiscip. Rev. - Nanomedicine Nanobiotechnology. 2 (2010) 77–87.

[3] N. Khlebtsov, L. Dykman, Biodistribution and toxicity of engineered gold nanoparticles: a review of in vitro and in vivo studies., Chem. Soc. Rev. 40 (2011) 1647–1671. doi:10.1039/c0cs00018c.

[4] D.B. Chithrani, Intracellular uptake, transport, and processing of gold nanostructures, Mol. Membr. Biol. 27 (2010) 299–311. doi:10.3109/09687688.2010.507787.

[5] K.P.M. Ricketts, U. Cheema, A. Nyga, A. Castoldi, C. Guazzoni, T. Magdeldin, et al., A 3D In Vitro Cancer Model as a Platform for Nanoparticle Uptake and Imaging Investigations, Small. (2014) 3954–3961. doi:10.1002/smll.201400194.

[6] G. Han, P. Ghosh, V.M. Rotello, Functionalized gold nanoparticles for drug delivery, Nanomedicine (Lond). 2 (2007) 113–123. doi:10.2217/17435889.2.1.113.

[7] B. F. Jiao, P.; Y. Zhou, H.; X. Chen, L.; Yan, Cancer-Targeting Multifunctionalized Gold Nanoparticles in Imaging and Therapy, Curr. Med. Chem. 18 (2011) 2086–2102.

[8] S. Jain, D.G. Hirst, J.M. O'Sullivan, Gold nanoparticles as novel agents for cancer therapy, Br. J. Radiol. 85 (2012) 101–113. doi:10.1259/bjr/59448833.

[9] J.F. Hainfeld, F.A. Dilmanian, Z. Zhong, D.N. Slatkin, J.A. Kalef-Ezra, H.M. Smilowitz, Gold nanoparticles enhance the radiation therapy of a murine squamous cell carcinoma., Phys. Med. Biol. 55 (2010) 3045–3059. doi:10.1088/0031-9155/55/11/004.

[10] Q. Chen, K. Li, S. Wen, H. Liu, C. Peng, H. Cai, et al., Targeted CT/MR dual mode imaging of tumors using multifunctional dendrimer-entrapped gold nanoparticles, Biomaterials. 34 (2013) 5200–5209. doi:10.1016/j.biomaterials.2013.03.009.

[11] J.F. Hainfeld, M.J. O'Connor, F.A. Dilmanian, D.N. Slatkin, D.J. Adams, H.M. Smilowitz, Micro-CT enables microlocalisation and quantification of Her2-targeted gold nanoparticles within tumour regions, Br. J. Radiol. 84 (2011) 526–533. doi:10.1259/bjr/42612922.

[12] A. Nyga, U. Cheema, M. Loizidou, 3D tumour models : novel in vitro approaches to cancer studies, J. Cell Commun. Signal. (2011) 239–248. doi:10.1007/s12079-011-0132-4.

[13] J.-K. Kim, S.-J. Seo, H.-T. Kim, K.-H. Kim, M.-H. Chung, K.-R. Kim, et al., Enhanced proton

treatment in mouse tumors through proton irradiated nanoradiator effects on metallic nanoparticles., Phys. Med. Biol. 57 (2012) 8309–23. doi:10.1088/0031-9155/57/24/8309.

[14] J.F. Hainfeld, D.N. Slatkin, T.M. Focella, H.M. Smilowitz, Gold nanoparticles: a new X-ray contrast agent, Br. J. Radiol. 79 (2006) 248–253. doi:10.1259/bjr/13169882.

[15] M.Y. Chang, A.L. Shiau, Y.H. Chen, C.J. Chang, H.H.W. Chen, C.L. Wu, Increased apoptotic potential and dose-enhancing effect of gold nanoparticles in combination with single-dose clinical electron beams on tumor-bearing mice, Cancer Sci. 99 (2008) 1479–1484. doi:10.1111/j.1349-7006.2008.00827.x.

[16] K. Ricketts, A Castoldi, C. Guazzoni, C. Ozkan, C. Christodoulou, A P. Gibson, G.J. Royle, A quantitative x-ray detection system for gold nanoparticle tumour biomarkers., Phys. Med. Biol. 57 (2012) 5543–55. doi:10.1088/0031-9155/57/17/5543.

[17] N. Manohar, F.J. Reynoso, S.H. Cho, Experimental demonstration of direct L-shell x-ray fluorescence imaging of gold nanoparticles using a benchtop x-ray source., Med. Phys. 40 (2013) 080702. doi:10.1118/1.4816297.

[18] K. Ricketts, C. Guazzoni, A Castoldi, A P. Gibson, G.J. Royle, An x-ray fluorescence imaging system for gold nanoparticle detection., Phys. Med. Biol. 58 (2013) 7841–55. doi:10.1088/0031-9155/58/21/7841.

[19] A. Thompson, X-ray data booklet, Centre for x-ray optics and advanced light source, Third Edit (2009).

[20] S.-K. Cheong, B.L. Jones, A.K. Siddiqi, F. Liu, N. Manohar, S.H. Cho, X-ray fluorescence computed tomography (XFCT) imaging of gold nanoparticle-loaded objects using 110 kVp x-rays., Phys. Med. Biol. 55 (2010) 647–662. doi:10.1118/1.3613446.

[21] D. Wu, Y. Li, M.D. Wong, H. Liu, A method of measuring gold nanoparticle concentrations by X-ray fluorescence for biomedical applications., Med. Phys. 40 (2013) 051901. doi:10.1118/1.4798966.

[22] L. Ren, D. Wu, Y. Li, G. Wang, X. Wu, H. Liu, Three-dimensional x-ray fluorescence mapping of a gold nanoparticle-loaded phantom, Med. Phys. 41 (2014) 31902. doi:10.1118/1.4863510.

[23] B.L. Jones, S.H. Cho, The feasibility of polychromatic cone-beam x-ray fluorescence computed tomography (XFCT) imaging of gold nanoparticle-loaded objects: a Monte Carlo study., Phys. Med. Biol. 56 (2011) 3719–30. doi:10.1088/0031-9155/56/12/017.

[24] G. Poludniowski, G. Landry, F. DeBlois, P.M. Evans, F. Verhaegen, SpekCalc: a program to calculate photon spectra from tungsten anode x-ray tubes., Phys. Med. Biol. 54 (2009) N433–8. doi:10.1088/0031-9155/54/19/N01.

[25] C. Chantler, K. Olsen, R. Dragoset, J. Chang, A. Kishore, S. Kotochigova, et al., X-Ray Form Factor, Attenuation and Scattering Tables (version 2.1), [Online] Available Http//physics.nist.gov/ffast. Natl. Inst. Stand. Technol. Gaithersburg, MD. (2005).

[26] G. Andermann, J.W. Kemp, Scattered X-Rays as Internal Standards in X-Ray Emission Spectroscopy, Anal. Chem. 30 (1958) 1306–1309.

[27] C. Bui, L. Confalonieri, M. Milazzo, Use of compton scattering in quantitative XRF analysis of stained glass, Int. J. Radiat. Appl. Instrumentation. Part A. Appl. Radiat. Isot. 40 (1989) 375–380. doi:10.1016/0883-2889(89)90200-1.

[28] B.L. Jones, N. Manohar, F. Reynoso, A. Karellas, S.H. Cho, Experimental demonstration of benchtop x-ray fluorescence computed tomography (XFCT) of gold nanoparticle-loaded objects using lead- and tin-filtered polychromatic cone-beams., Phys. Med. Biol. 57 (2012) N457–67. doi:10.1088/0031-9155/57/23/N457.